

Optimization-Based Visual-Inertial SLAM Tightly Coupled with Raw GNSS Measurements

Jinxu Liu, Wei Gao* and Zhanyi Hu

Abstract—Fusing vision, Inertial Measurement Unit (IMU) and Global Navigation Satellite System (GNSS) information is a promising solution for accurate global positioning in complex urban scenes, because of the complementarity of the different sensors. Unlike the loose coupling approaches and the EKF-based approaches in the literature, we propose an optimization-based visual-inertial SLAM tightly coupled with raw GNSS measurements, including pseudoranges and Doppler shift, which is the first of such approaches to our knowledge. Reprojection error, IMU pre-integration error and raw GNSS measurement error are jointly optimized using bundle adjustment in a sliding window, and the asynchronism between images and raw GNSS measurements is considered. Marginalization is performed in the sliding window, and some methods dealing with noisy measurements and vulnerable situations are employed. Experimental results on public dataset in complex urban scenes prove that our proposed approach outperforms state-of-the-art visual-inertial SLAM, GNSS single point positioning, as well as a loose coupling approach, both in the scenes that mainly contain low-rise buildings and the scenes that contain urban canyons.

I. INTRODUCTION

Positioning in outdoor scenes has long been a concerned task by the researchers in the realms of autonomous driving, unmanned aerial vehicles and large-scale augmented reality. Global Navigation Satellite System (GNSS) has been widely exploited for decades, due to its ability to acquire geodetic coordinates and its stable performance in open area. However, in *urban canyons* where there are lots of skyscrapers in the surroundings, GNSS positioning results dramatically deteriorate because most of the GNSS signals are blocked or reflected. On the other hand, camera and Inertial Measurement Unit (IMU) do not suffer from urban canyons, and visual SLAM (V-SLAM) and visual inertial SLAM (VI-SLAM) perform well if the scene has abundant texture and not too many moving objects. What's more, the local accuracy of V-SLAM or VI-SLAM approaches is much higher than that of single point GNSS positioning, due to the fact that the current pose is always computed depending on previous poses in SLAM approaches.

Nevertheless, V-SLAM and VI-SLAM approaches also have their inherent shortcomings. Besides the deterioration of accuracy in low-textured scenes and the scenes with many moving objects, the SLAM approaches suffer from drift and

thus have lower global accuracy, as some directions of the parameters are unobservable. And more importantly, since global position is unobservable for SLAM approaches, what can be obtained from SLAM approaches are the poses relative to the starting point, which need to be transformed into geodetic coordinate frame with the aid of additional global information provided by other sensors, such as GNSS. Hence GNSS positioning and V-SLAM or VI-SLAM approaches are complementary, because of their different global and local accuracy, as well as their different vulnerable scenes.

II. RELATED WORK

A. Loose Coupling Approaches

Loose coupling approaches firstly derive poses from feature points, or the positions and velocities from raw GNSS measurements, or both of the above two quantities. Then some the derived quantities rather than raw measurements are involved in the fusion stage, which generally adopts either Extended Kalman Filter (EKF) or optimization framework. Some approaches [1], [2] derive poses from feature points, and fuse them with raw GNSS measurements such as pseudorange and Doppler shift, where loose coupling is applied on the vision side. Conversely, some approaches [3], [4] derive positions from raw GNSS measurements, and fuse them with feature points from the images, where loose coupling is applied on the GNSS side. Other approaches [5], [6], [7], [8] apply loose coupling on both the vision side and the GNSS side, i.e. the derived visual quantities and the derived GNSS quantities are involved in the fusion stage. In addition, there are approaches [2], [9] where visual information is exploited to aid GNSS positioning by judging which satellites are visible. The above loose coupling approaches are not optimal. For example, when the GNSS measurements are in good quality but the GNSS satellites are poorly distributed, the loose coupling approaches will deteriorate because the derived GNSS quantities are inaccurate, but the tight coupling approaches are not affected under such conditions.

B. Tight Coupling Approaches

This category of approaches employs tight coupling on both the vision side and the GNSS side. That is to say, both the feature points from the image and the raw GNSS measurements such as pseudorange and Doppler shift serve as measurements either in an EKF-based or in an optimization-based framework. The EKF-based approaches [10], [11] tightly couple vision, IMU and single point GNSS. They perform state prediction using the IMU measurements, and

This work was supported in part by the National Key R&D Program of China (2016YFB0502002), and in part by the Natural Science Foundation of China (61872361). *Corresponding Author: Wei Gao wgao@nlpr.ia.ac.cn.

All authors are with National Laboratory of Pattern Recognition, Institute of Automation, Chinese Academy of Sciences, and with School of Artificial Intelligence, University of Chinese Academy of Sciences, China.

update the states using the feature points as well as the pseudorange and Doppler shift measurements. Similar EKF-based framework is adopted in [12], while [12] utilizes double-differenced GNSS instead of single point GNSS, and hence double-differenced pseudorange and double-differenced carrier phase are utilized as measurements for state update, instead of the directly measured pseudorange and Doppler shift. Double-differenced GNSS provides measurements for more accurate positioning, but requires an additional base station in comparison with single point GNSS.

Besides EKF-based approaches, optimization-based sensor fusion approaches are emerging as well. Compared with EKF, batch optimization allows for the reduction of error through relinearization in visual-inertial navigation systems [13] and proves to have better performance in GNSS-IMU fusion task [14]. Therefore, optimization is a promising solution to fuse vision, IMU and GNSS measurements. The optimization-based approach [15] tightly couples feature points with pseudorange from single point GNSS in bundle adjustment. However, Doppler shift is not utilized, and IMU measurements are not tightly coupled in [15], and only the magnetometer in IMU is exploited, to determine the direction of the local world frame. Nevertheless, tightly coupling IMU measurements can eliminate the effect of the asynchronism between vision and GNSS measurements, thus the low-speed motion assumption applied in [15] is not needed in this case.

In this paper we propose an approach that tightly couples vision, IMU and single point raw GNSS measurements including pseudoranges and Doppler shift in an optimization-based framework, which is the first of such approaches to our knowledge.

III. PRELIMINARIES

A. Frames and Notations

In this paper, the world frames include the earth-centered, earth-fixed (ECEF) frame, the ground east-north-up (ENU) frame, and the local world frame for SLAM. The sensor frames include the camera frame, the IMU frame and the GNSS receiver frame. The above world frames and sensor frames are illustrated in Fig.1. We use $(\cdot)^{WE}$, $(\cdot)^{WG}$ and $(\cdot)^{WL}$ to denote the ECEF frame, the ground ENU frame and the local world frame for SLAM respectively, and use $(\cdot)^c$, $(\cdot)^b$ and $(\cdot)^g$ to denote the camera frame, IMU frame and GNSS receiver frame respectively. Specially, we use $(\cdot)^{b_k}$ and $(\cdot)^{g_k}$ to denote the IMU frame and GNSS receiver frame corresponding to the k^{th} image, and slightly abuse the symbols using $(\cdot)^{b_t}$ and $(\cdot)^{g_t}$ to denote the IMU frame and GNSS receiver frame at some moment t .

Let \mathbf{R}_A^B denote the rotation matrix that takes a vector in frame $\{A\}$ to frame $\{B\}$, and \mathbf{q}_A^B is its quaternion form. \mathbf{p}_A^B is the coordinate of the origin point of frame $\{A\}$ in frame $\{B\}$, and \mathbf{v}_A^B is the velocity of the origin point of frame $\{A\}$ measured in frame $\{B\}$. Note that for GNSS receiver frame, only the coordinate of its origin point in frame $\{WL\}$ matters in our approach, and the orientations of its axes can be regarded as arbitrary. Let \mathbf{b}_{a_k} and \mathbf{b}_{ω_k} denote the accelerometer bias and gyroscope bias corresponding to

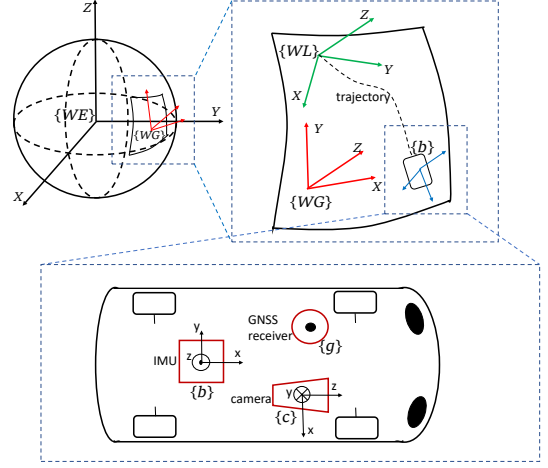


Fig. 1. Illustration of world frames and sensor frames. The globe in the upper left of the figure is the earth globe. The origin of the ECEF frame $\{WE\}$ is on the center of the earth. The X axis of the ECEF frame points to the point of intersection between the prime meridian and equator, and the Z axis points to the North Pole. The ground ENU frame $\{WG\}$ and the local world frame for SLAM $\{WL\}$ both locate on the ground, with their Z axes pointing upward.

image k respectively. Moreover, we use $[\cdot]_{\times}$ to denote the skew symmetric matrix corresponding to a vector.

B. GNSS Single Point Positioning and Velocity Measurement

GNSS single point positioning and velocity measurement are used in GNSS-SLAM initialization in Sect.IV-A and filtering out the noisy GNSS measurements in Sect.IV-D. For single point positioning, the states to be estimated include

$$\mathcal{X}^P = [\mathbf{p}_g^{WE}, \delta t_0^r \dots \delta t_{J-1}^r], \quad (1)$$

where J is the number of different GNSS constellations, such as GPS, GLONASS, etc. δt_j^r for $j = 0 \dots J-1$ is the receiver clock bias w.r.t. GNSS constellation j . The cost function $c^P(\mathcal{X}^P)$ that is to be minimized can be written as

$$c^P(\mathcal{X}^P) = \sum_{i=0}^{N-1} \|\mathbf{e}_i^P\|^2, \quad (2)$$

where N is the number of observed satellites and

$$\mathbf{e}_i^P = \|\mathbf{p}_{s_i}^{WE} - \mathbf{p}_g^{WE}\| + c\delta t_{j(i)}^r - c\delta t_i^s - \rho_i, \quad (3)$$

where c is the light speed, $\mathbf{p}_{s_i}^{WE}$ and δt_i^s are the position in ECEF frame and clock bias of satellite i respectively, which are computed directly from the broadcast ephemeris. The subscript $j(i)$ means the constellation corresponding to satellite i , and ρ_i is the pseudorange measurement after ionospheric delay correction and tropospheric delay correction.

For velocity measurement, the states to be estimated include

$$\mathcal{X}^D = [\mathbf{v}_g^{WE}, \delta t_0^r \dots \delta t_{J-1}^r], \quad (4)$$

where J is the number of different GNSS constellations, and δt_j^r for $j = 0 \dots J-1$ is the receiver clock drift w.r.t. GNSS constellation j . The cost function $c^D(\mathcal{X}^D)$ can be written as

$$c^D(\mathcal{X}^D) = \sum_{i=0}^{N-1} \|\mathbf{e}_i^D\|^2, \quad (5)$$

where N is the number of observed satellites and

$$\mathbf{e}_i^D = \mathbf{I}_i^T (\mathbf{v}_{s_i}^{WE} - \mathbf{v}_g^{WE}) + c\delta t_{j(i)}^r - (-\lambda_i D_i), \quad (6)$$

where $\mathbf{v}_{s_i}^{WE}$ and δt_i^s are the velocity in ECEF frame and clock drift of satellite i respectively, which are computed directly from the broadcast ephemeris. λ_i and D_i are the wavelength of the carrier and the Doppler shift measurement respectively. \mathbf{I}_i^T is computed as $\mathbf{I}_i^T = \frac{\mathbf{p}_{s_i}^{WE} - \mathbf{p}_g^{WE}}{\|\mathbf{p}_{s_i}^{WE} - \mathbf{p}_g^{WE}\|}$ leveraging \mathbf{p}_g^{WE} computed through single point positioning. The meanings of c and subscript $j(i)$ are the same as those in (3).

IV. METHOD

A. GNSS-SLAM Initialization

After our system starts, the initialization for VI-SLAM is performed, and the nonlinear optimization for VI-SLAM starts performing temporarily following the routine of [16]. Meanwhile, the GNSS single point positioning is performed as described in Sect. III-B. Hence we have obtained the VI-SLAM trajectory and the GNSS single point positioning trajectory respectively. At GNSS-SLAM initialization stage we align the above two trajectories, in order to compute the value of \mathbf{R}_{WG}^{WE} and \mathbf{p}_{WG}^{WE} , as well as the initial value of \mathbf{R}_{WL}^{WG} and \mathbf{p}_{WL}^{WG} .

Firstly, we select one position calculated by GNSS single point positioning as the reference point \mathbf{p}_{ref}^{WE} , which serves as the origin point of the ground ENU frame. In our implementation, the third GNSS single point positioning result since the system starts is selected as the reference point. Given the reference point, \mathbf{R}_{WG}^{WE} and \mathbf{p}_{WG}^{WE} can be computed straightforwardly. We have $\mathbf{p}_{WG}^{WE} = \mathbf{p}_{ref}^{WE}$, and

$$\mathbf{R}_{WG}^{WE} = \begin{bmatrix} -\sin \lambda & \cos \lambda & 0 \\ -\sin \phi \cos \lambda & -\sin \phi \sin \lambda & \cos \phi \\ \cos \phi \cos \lambda & \cos \phi \sin \lambda & \sin \phi \end{bmatrix}^T, \quad (7)$$

where ϕ and λ are the latitude and longitude of the reference point respectively, which can be easily converted from the ECEF position \mathbf{p}_{ref}^{WE} [17]. Then the GNSS single point positioning trajectory is converted from the ECEF frame to the ground ENU frame as

$$\mathbf{p}_g^{WG} = \mathbf{R}_{WG}^{WE^T} (\mathbf{p}_g^{WE} - \mathbf{p}_{WG}^{WE}). \quad (8)$$

Hence we have two sets of positions $\{\mathbf{p}_{gl}^{WG} | l = 0 \dots L-1\}$ and $\{\mathbf{p}_{bl}^{WL} | l = 0 \dots L-1\}$, of which the former includes the positions from GNSS single point positioning in frame $\{WG\}$, and the latter includes the positions estimated from VI-SLAM in frame $\{WL\}$. Note that the positions from VI-SLAM are in fact \mathbf{p}_{bl}^{WL} , but at the initialization stage we neglect the translation from IMU frame to GNSS receiver frame, thus we regard \mathbf{p}_{bl}^{WL} as \mathbf{p}_{gl}^{WL} . At this stage interpolation is performed to align the timestamps of the above two sets of positions. At last a 5-Degrees of Freedom(DoF) alignment between the above two sets is performed to compute the initial value of \mathbf{R}_{WL}^{WG} and \mathbf{p}_{WL}^{WG} , which writes as

$$\min_{s, \mathbf{R}_{WL}^{WG}, \mathbf{p}_{WL}^{WG}} \sum_{l=0}^{L-1} \|\mathbf{p}_{gl}^{WG} - s\mathbf{R}_{WL}^{WG}\mathbf{p}_{gl}^{WL} - \mathbf{p}_{WL}^{WG}\|^2. \quad (9)$$

The scale parameter s is estimated because the VI-SLAM is prone to suffer from scale drift in degenerate cases[18]. Note that \mathbf{R}_{WL}^{WG} only contains one DoF, which is the rotation around Z axis, because the Z axes of both frame $\{WG\}$ and frame $\{WL\}$ point upward. The initial value of \mathbf{p}_{WL}^{WG} is solved by centering the two sets of positions, and the initial value of \mathbf{R}_{WL}^{WG} is obtained by searching every 1 degree after centering, followed by solving the minimization problem (9) iteratively. After minimization, \mathbf{p}_{WL}^{WG} is adjusted according to the estimated s because the scaling factor s is not applied in the following stages.

B. Tightly Coupled Optimization

After GNSS-SLAM initialization, raw GNSS measurements, i.e. pseudoranges and Doppler shift, are integrated into optimization. The states to be estimated include

$$\mathcal{X} = [\mathbf{x}_0 \dots \mathbf{x}_{K-1}, f_0 \dots f_{M-1}, \mathbf{T}_c^b, \mathbf{T}_{WL}^{WG}, \delta \mathbf{t}_0^r \dots \delta \mathbf{t}_{E-1}^r, \delta \mathbf{t}_0^r \dots \delta \mathbf{t}_{E-1}^r], \quad (10)$$

where K is the number of images in the sliding window, M is the number of landmarks, and E is the number of GNSS epochs in the sliding window. f is the inverse depth of one landmark in camera frame, and

$$\begin{aligned} \mathbf{x}_k &= [\mathbf{p}_{b_k}^{WL}, \mathbf{v}_{b_k}^{WL}, \mathbf{q}_{b_k}^{WL}, \mathbf{b}_{a_k}, \mathbf{b}_{\omega_k}], k = 0 \dots K-1, \\ \mathbf{T}_c^b &= [\mathbf{R}_c^b, \mathbf{p}_c^b], \mathbf{T}_{WL}^{WG} = [\mathbf{R}_{WL}^{WG}, \mathbf{p}_{WL}^{WG}], \\ \delta \mathbf{t}_e^r &= [\{\delta t_{j,e}^r | \forall j \in \mathcal{O}(e)\}], e = 0 \dots E-1, \\ \delta \mathbf{t}_e^r &= [\{\delta t_{j,e}^r | \forall j \in \mathcal{O}(e)\}], e = 0 \dots E-1, \end{aligned} \quad (11)$$

where $\mathcal{O}(e)$ is the set of observable GNSS constellations at epoch e , $\delta t_{j,e}^r$ and $\delta t_{j,e}^r$ are the receiver clock bias and clock drift w.r.t GNSS constellation j at epoch e respectively, and $\delta \mathbf{t}_e^r$ and $\delta \mathbf{t}_e^r$ are the vectors containing the receiver clock biases and clock drifts for all the observable constellations at epoch e respectively. Compared with VINS-mono[16], the introduced additional parameters include the transformation from the local world frame to ground ENU frame, as well as clock biases and clock drifts. The transformation from ground ENU frame to ECEF frame ($\mathbf{R}_{WG}^{WE}, \mathbf{p}_{WG}^{WE}$) is treated as a known quantity rather than a parameter, because the ground ENU frame can be located anywhere on the ground that is not too far away from the current position. Although GNSS measurements and images are collected at different moments, we do not introduce additional parameters concerning pose and velocity at GNSS measurement moments. In other words, we incorporate intermediate GNSS measurements, which is inspired by [19]. Note that just like in the GNSS-SLAM initialization stage, \mathbf{R}_{WL}^{WG} only has 1 DoF, so it is parameterized only by the rotation angle around the Z axis, which writes as κ_{WL}^{WG} .

The cost function $c(\mathcal{X})$ that is to be minimized writes as

$$\begin{aligned} c(\mathcal{X}) &= c^{reproj}(\mathcal{X}) + c^{IMU}(\mathcal{X}) + \sum_{e=0}^{E-1} \sum_{i \in \mathcal{I}(e)} \mathbf{e}_{i,e}^p{}^T \mathbf{W}^p \mathbf{e}_{i,e}^p \\ &\quad + \sum_{e=0}^{E-1} \sum_{i \in \mathcal{I}(e)} \mathbf{e}_{i,e}^d{}^T \mathbf{W}^d \mathbf{e}_{i,e}^d + \mathbf{e}^{margT} \mathbf{e}^{marg}, \end{aligned} \quad (12)$$

where E is the number of GNSS epochs in the sliding window and $\mathcal{S}(e)$ is the set of observable GNSS satellites at epoch e . $\mathbf{e}_{i,e}^P$ and $\mathbf{e}_{i,e}^D$ are the pseudorange residual and the Doppler shift residual for satellite i observed at epoch e respectively. \mathbf{e}^{marg} denotes the marginalization residual. The reprojection factors $c^{reproj}(\mathcal{X})$ and IMU factors $c^{IMU}(\mathcal{X})$ are identical to those in VINS-mono[16], and the readers may refer to (14), (16) and (17) in VINS-mono[16] for details. The IMU pre-integration performed in our proposed approach is also identical to that in VINS-mono[16].

As for the GNSS factors, the pseudorange residual $\mathbf{e}_{i,e}^P$ and the Doppler shift residual $\mathbf{e}_{i,e}^D$ write as

$$\begin{aligned}\mathbf{e}_{i,e}^P &= \|\mathbf{p}_{s_i,e}^{WE} - (\mathbf{R}_{WG}^{WE} \mathbf{R}_{WL}^{WG} \mathbf{p}_{g_{m(e)}}^{WL} + \mathbf{R}_{WG}^{WE} \mathbf{p}_{WL}^{WG} + \mathbf{p}_{WG}^{WE})\| + c\delta t_{j(i),e}^r \\ &\quad - c\delta t_{i,e}^s - \rho_{i,e}, \\ \mathbf{e}_{i,e}^D &= \mathbf{l}_{i,e}^T (\mathbf{v}_{s_i,e}^{WE} - \mathbf{R}_{WG}^{WE} \mathbf{R}_{WL}^{WG} \mathbf{v}_{g_{m(e)}}^{WL}) + c\delta t_{j(i),e}^r - c\delta t_{i,e}^s - (-\lambda_{i,e} D_{i,e}),\end{aligned}\quad (13)$$

where

$$\begin{aligned}\mathbf{l}_{i,e} &= \frac{\mathbf{p}_{s_i,e}^{WE} - (\mathbf{R}_{WG}^{WE} \mathbf{R}_{WL}^{WG} \mathbf{p}_{g_{m(e)}}^{WL} + \mathbf{R}_{WG}^{WE} \mathbf{p}_{WL}^{WG} + \mathbf{p}_{WG}^{WE})}{\|\mathbf{p}_{s_i,e}^{WE} - (\mathbf{R}_{WG}^{WE} \mathbf{R}_{WL}^{WG} \mathbf{p}_{g_{m(e)}}^{WL} + \mathbf{R}_{WG}^{WE} \mathbf{p}_{WL}^{WG} + \mathbf{p}_{WG}^{WE})\|}, \\ \mathbf{p}_{g_{m(e)}}^{WL} &= \mathbf{p}_{b_k}^{WL} + \mathbf{v}_{b_k}^{WL} \Delta t_{k,m(e)} + \mathbf{R}_{b_k}^{WL} (\boldsymbol{\alpha}_{b_{m(e)}}^{b_k} + \mathbf{R}(\boldsymbol{\gamma}_{b_{m(e)}}^{b_k}) \mathbf{p}_g^b) \\ &\quad - \frac{1}{2} \mathbf{g}^{WL} \Delta t_{k,m(e)}^2, \\ \mathbf{v}_{g_{m(e)}}^{WL} &= \mathbf{v}_{b_k}^{WL} + \mathbf{R}_{b_k}^{WL} (\boldsymbol{\beta}_{b_{m(e)}}^{b_k} - \mathbf{R}(\boldsymbol{\gamma}_{b_{m(e)}}^{b_k}) [\mathbf{p}_g^b] \times (\hat{\boldsymbol{\omega}}_{m(e)} - \mathbf{b}_{\omega_k})) \\ &\quad - \mathbf{g}^{WL} \Delta t_{k,m(e)}.\end{aligned}\quad (14)$$

In (13) and (14), $\mathbf{p}_{s_i,e}^{WE}$ and $\delta t_{i,e}^s$ are the position and clock bias of satellite i at GNSS epoch e respectively, and $\mathbf{v}_{s_i,e}^{WE}$ and $\delta t_{i,e}^s$ are the velocity and clock drift of satellite i at epoch e respectively. The above four quantities are computed directly from the broadcast ephemeris. The subscript $m(e)$ denotes the measurement moment of GNSS epoch e . The subscript $j(i)$ is the GNSS constellation corresponding to satellite i , hence the parameters $\delta t_{j(i),e}^r$ and $\delta t_{j(i),e}^s$ are the receiver clock bias and clock drift w.r.t GNSS constellation $j(i)$ at epoch e respectively. $\rho_{i,e}$, $\lambda_{i,e}$ and $D_{i,e}$ are the pseudorange measurement, wavelength of the carrier, and Doppler shift measurement of satellite i at epoch e respectively. c is the light speed, and $\Delta t_{k,m(e)}$ is the time interval from the exposure moment of image k to the moment $m(e)$. \mathbf{p}_g^b is the translational component of IMU-GNSS receiver extrinsic parameters, which is assumed to have been accurately calibrated beforehand in this paper. $\boldsymbol{\alpha}_{b_{m(e)}}^{b_k}$, $\boldsymbol{\beta}_{b_{m(e)}}^{b_k}$ and $\boldsymbol{\gamma}_{b_{m(e)}}^{b_k}$ are the nominal states coming from IMU pre-integration from the exposure moment of image k to the moment $m(e)$, and they correspond to displacement, change in velocity, and relative rotation respectively. $\mathbf{R}(\boldsymbol{\gamma}_{b_{m(e)}}^{b_k})$ is the rotation matrix converted from the rotation quaternion $\boldsymbol{\gamma}_{b_{m(e)}}^{b_k}$. For the details of IMU-preintegration the readers may refer to (3) and (5) in VINS-mono[16]. $\hat{\boldsymbol{\omega}}_{m(e)}$ is the angular velocity measurement from IMU at moment $m(e)$, and \mathbf{g}^{WL} is the gravity vector in frame $\{WL\}$, which writes as $[0 \ 0 \ g]^T$ with g being the magnitude of gravity. In (14), an approximation is applied that the gyroscope bias at image exposure moment \mathbf{b}_{ω_k}

substitutes for the gyroscope bias at GNSS measurement moment $m(e)$, because gyroscope bias is a slow time-varying quantity.

In fact, \mathbf{W}^P and \mathbf{W}^D in (12) are both 1×1 matrices which can be regarded as scalars. In our implementation, we adopt $\mathbf{W}^P = 1$ and $\mathbf{W}^D = 4$, supposing the median errors of pseudorange measurements and pseudorange rates converted from Doppler shift measurements to be $1m$ and $0.5m/s$ respectively. The optimization is performed in a sliding window minimizing the cost function $c(\mathcal{X})$ using Ceres Solver[20].

C. Sliding Window and Marginalization

In the sliding window in our approach illustrated in Fig.2, the parameters related to GNSS, i.e. GNSS receiver clock bias and clock drift, are *attached* to the image frame just before it. There may exist more than one GNSS parameter node attached to a certain image frame.

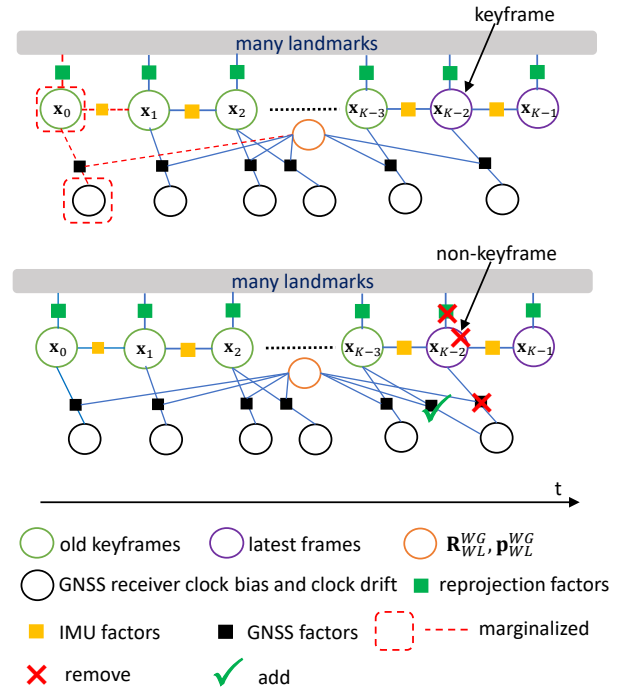


Fig. 2. Marginalization in sliding window. The hollow circles represent the parameters (nodes), and the solid rectangles represent the factors (edges). The camera-IMU extrinsic parameters and the marginalization factor are not shown here for clarity of explanation.

If the second latest frame is a keyframe, we keep it in the sliding window, and marginalize the oldest keyframe and the GNSS parameters and feature points attached to it, as well as the reprojection factors, IMU factors and GNSS factors related to them. If the second latest frame is not a keyframe, we simply remove the frame and all its corresponding visual measurements. However, the GNSS parameters attached to the second latest frame will not be removed, and they will be attached to the third latest frame instead, i.e. removed and added in Fig.2. The GNSS factors that are originally attached to the second latest frame will be changed, for

the reason that the IMU pre-integration in the above GNSS factors need to be recomputed because their starting moments will switch from the second latest frame to the third latest frame. The GNSS measurements in the above GNSS factors remain unchanged.

The marginalization in our approach is carried out using Schur-Complement. The readers may refer to [21] and [16] for details of applying marginalization.

D. Methods Dealing with Noisy Measurements and Vulnerable Situations

- In urban canyons, raw GNSS measurement can be pretty noisy. Therefore, before the GNSS measurements enter into the sliding window for optimization, we perform single point positioning and velocity measurement as described in Sect.III-B, and compute the residuals of pseudoranges and Doppler shift measurements. The pseudoranges and Doppler shifts are filtered out if their corresponding residuals exceed the threshold T^P and T^D respectively. If too few GNSS measurements are left after filtering out the noisy measurements at a certain GNSS epoch, we will filter out all the GNSS measurements at the epoch altogether. In our implementation, $T^P = 10m$ and $T^D = 3m/s$. Fig.3 shows the GNSS single point positioning results and the results of our filtering operation. From Fig.3 we can see that the GNSS epochs when measurements are all filtered out generally experience less accurate single point positioning results than the epochs when measurements are partially filtered out or not filtered out.

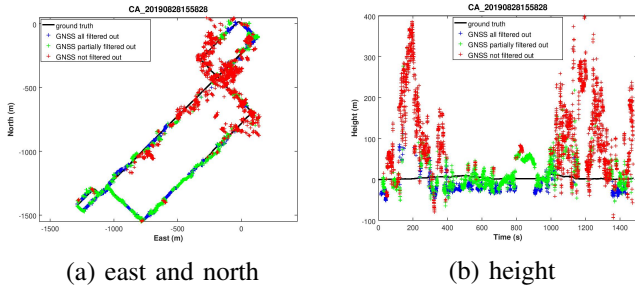


Fig. 3. GNSS single point positioning results w.r.t east and north directions (a), and w.r.t height direction (b). The red, green and blue markers are epochs when GNSS measurements are all filtered out, partially filtered out and not filtered out respectively. The single point positioning is performed as described in Sect. III-B.

- From the above single point positioning, the GNSS receiver clock bias can be estimated. The estimated clock bias serves as initial value for the clock bias parameters in (10).
- At the initial stage just after GNSS-SLAM initialization, a prior factor constraining the parameters ($\mathbf{R}_{WL}^{WG}, \mathbf{p}_{WL}^{WG}$) is added to the sliding window, because at the initial stage the marginalization factor does not contain enough information from GNSS measurements in the past, and thus the estimation of ($\mathbf{R}_{WL}^{WG}, \mathbf{p}_{WL}^{WG}$) is susceptible to noises in GNSS measurements. After the GNSS factors

in more than T^N GNSS epochs have been marginalized, the prior factor is permanently removed from the sliding window. Note that the prior factor is not marginalized, hence it will not take any effect since it is removed.

The prior residual writes as $\mathbf{e}^{prior} = \begin{bmatrix} w(\mathbf{p}_{WL}^{WG} - \hat{\mathbf{p}}_{WL}^{WG}) \\ w(\mathbf{\kappa}_{WL}^{WG} - \hat{\mathbf{\kappa}}_{WL}^{WG}) \end{bmatrix}$, where \mathbf{p}_{WL}^{WG} is parameter in (10), and $\mathbf{\kappa}_{WL}^{WG}$ is the rotation around Z axis used to parameterize \mathbf{R}_{WL}^{WG} in (10). $\hat{\mathbf{p}}_{WL}^{WG}$ and $\hat{\mathbf{\kappa}}_{WL}^{WG}$ are estimated from GNSS-SLAM initialization in Sect.IV-A. In our implementation, $T^N = 30$ and the weight $w = 15$.

- Since the accuracy of IMU-preintegration decreases as the time interval for pre-integration increases, any GNSS factor that is more than T^t seconds later than the image frame it attaches to is simply removed from the sliding window. In this way we can avoid the inaccuracy of the IMU-preintegration results in GNSS factors (see (14)). In our implementation the raw GNSS measurements come at a frequency of about 4Hz, hence we choose $T^t = 2$.
- According to [18] and [22], VI-SLAM system is not well-constrained before the platform has made a turn for the first time. Therefore, we employ the strategy proposed in [22] but in a much simpler way that we start to adjust the camera-IMU extrinsic parameters ($\mathbf{R}_c^b, \mathbf{p}_c^b$) in optimization after the platform has made a turn.
- In our experiments, we find that it is a vulnerable scene for our approach when the car stops at a crossroad, which may be due to the fact that the accuracy of IMU pre-integration between two keyframes decreases as the time interval between two keyframes increases. In our implementation when the estimated speed of the second latest frame is under $0.5m/s$, the GNSS factors in the sliding window are temporarily *removed*, but they still participate in marginalization as if they were in the sliding window.

V. EXPERIMENTS

The experiments are conducted on the public dataset UrbanLoco[23], which is collected in highly urbanized areas in San Francisco and Hong Kong. The images in Hong Kong data are collected using a fisheye sky camera, and the images in San Francisco data are collected using six 360-degree view cameras. Our approach is evaluated on 4 sequences collected in San Francisco, because VINS-mono[16] evaluation results on only the above 4 sequences are reported in the paper [23]. The 4 sequences contain both urban canyons and scenes with low-rise buildings, which are shown in Fig.4. All the experiments presented are performed on a PC with Intel Core i7 3.6GHz×6 core CPU and 64GB memory.

Our proposed approach is compared with state-of-the-art VI-SLAM approach VINS-mono[16], GNSS single point positioning results computed using RTKLIB[24], and the loose coupling approach VINS-Fusion (with GNSS)[8]. The accuracies of the above approaches are compared in Table I. In Table I, the evaluation results of VINS-mono[16] are the reported results in [23], and the other three approaches

TABLE I
COMPARISON OF MEAN ABSOLUTE ERROR (MAE) OF RESULTING TRAJECTORIES FROM DIFFERENT APPROACHES

Data Sequence	Length (km)	Method	MAE in Translation (m)			MAE in Rotation (deg)		
			X	Y	Z	Z	Y	X
CA_20190828155828	5.9	VINS-mono[16]	42.68	42.68	23.24	6.04	0.69	2.05
		GNSS SPP	6.294	5.269	11.956	*	*	*
		VINS-Fusion (with GNSS)[8]	11.591	9.256	33.936	5.225	10.724	11.816
		Proposed	7.093	7.722	8.261	1.494	0.352	2.134
CA_20190828173350	3.2	VINS-mono[16]	26.745	34.756	14.83	8.12	0.81	2.47
		GNSS SPP	88.003	48.294	181.261	*	*	*
		VINS-Fusion (with GNSS)[8]	15.688	15.799	30.165	21.387	26.595	16.871
		Proposed	5.539	12.811	7.884	1.646	0.620	2.210
CA_20190828184706	1.8	VINS-mono[16]	32.52	31.47	26.89	2.65	0.89	1.28
		GNSS SPP	2.270	2.190	5.514	*	*	*
		VINS-Fusion (with GNSS)[8]	2.120	2.729	4.519	6.130	15.166	9.207
		Proposed	1.881	1.656	0.668	4.287	0.470	2.073
CA_20190828190411	1.0	VINS-mono[16]	22.27	17.57	23.84	11.32	4.12	4.31
		GNSS SPP	5.408	3.441	9.310	*	*	*
		VINS-Fusion (with GNSS)[8]	7.585	3.103	8.542	9.320	8.961	7.929
		Proposed	3.693	3.187	2.982	2.965	0.911	2.058

Here *GNSS SPP* means GNSS single point positioning. *Proposed* means the proposed approach in this paper. The symbol * means the result is not available. GNSS single point positioning only provides positioning results, hence its rotational accuracy is not available.



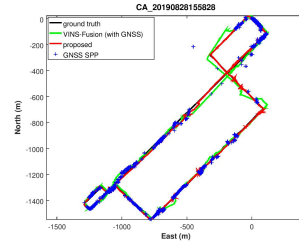
(a) urban canyon



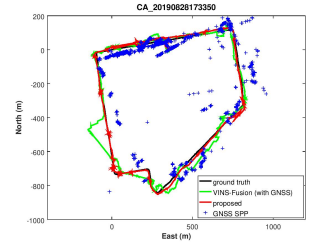
(b) low-rise buildings

Fig. 4. Urban canyon (a) and low-rise buildings (b) in the sequences on which the experiments are conducted.

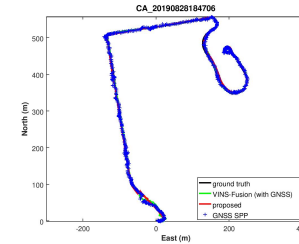
are evaluated by ourselves. *GNSS SPP* is the single point positioning result produced using RTKLIB[24]. For VINS-Fusion (with GNSS)[8], the inputted GNSS positions are the single point positioning results from RTKLIB[24], i.e. the results of *GNSS SPP*. For fairness of comparison, we employ the frontal camera and the IMU in both VINS-Fusion (with GNSS)[8] and our proposed approach. Also for fairness of comparison, because the resulting trajectory of VINS-mono[16] is aligned to the ground truth by a rigid body transformation[25] before evaluation in paper [23], the other three approaches are also aligned to the ground truth by a rigid body transformation before evaluation. For each approach the loop closure option is turned off. For *GNSS SPP* and our proposed approach, the same raw GNSS measurements are utilized, including the measurements from both GPS and GLONASS. Same as the evaluation of VINS-mono[16] in paper [23], our proposed approach is also evaluated at about half-real time playback rate. The comparisons of trajectories among different approaches w.r.t the east and north directions, as well as w.r.t. the height direction are also shown in Fig.5 and Fig.6 respectively. From Table I, Fig.5 and Fig.6 we can see that our proposed approach



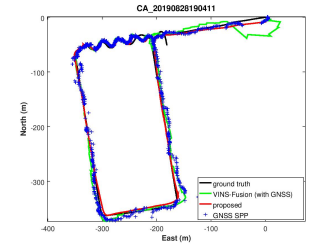
(a) CA_20190828155828



(b) CA_20190828173350



(c) CA_20190828184706



(d) CA_20190828190411

Fig. 5. Comparison of trajectories in east and north directions. In figure (b) a few very noisy GNSS SPP results that lie outside the figure are omitted. All trajectories are aligned with the ground truth.

outperforms the other three approaches w.r.t the accuracy of both translation and rotation.

Tightly coupling raw GNSS measurements, our approach achieves global positioning results. For our proposed approach, the resulting trajectories of two sequences are projected onto the Google Map, which are shown in Fig.7.

VI. CONCLUSIONS

In this paper, we propose an optimization-based visual-inertial SLAM tightly coupled with raw GNSS measurements. Feature points, IMU measurements as well as pseudo-ranges and Doppler shift measurements from GNSS, which

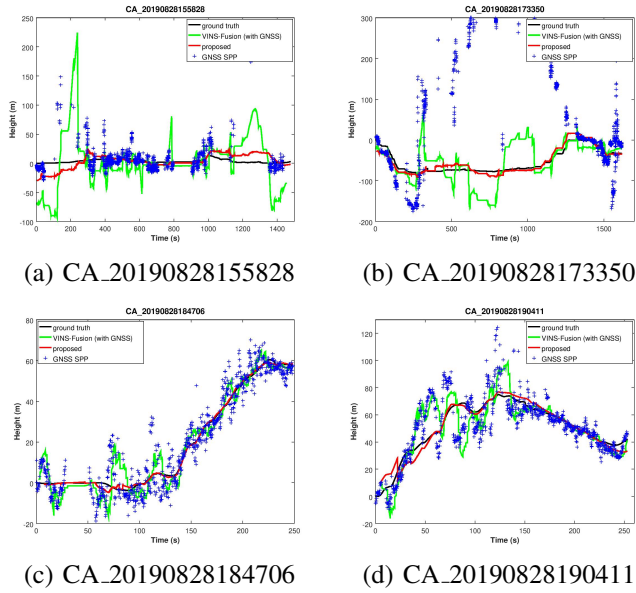


Fig. 6. Comparison of trajectories in height direction. In figure (a) and (b) a few very noisy GNSS SPP results that lie outside the figure are omitted. All trajectories are aligned with the ground truth.



Fig. 7. Our resulting trajectories of (a) CA_20190828184706 and (b) CA_20190828190411 projected onto Google Map.

are captured at different moments, are integrated by means of optimization in a sliding window. Experimental results prove that our proposed approach outperforms standard visual-inertial SLAM, GNSS single point positioning, as well as the loose coupling approach [8] on public dataset. In the future, approaches that aid the mapping process in the backend with raw GNSS measurements may be explored.

REFERENCES

- [1] M. Schreiber, H. Königshof, A. Hellmund, and C. Stiller. Vehicle localization with tightly coupled gnss and visual odometry. In *2016 IEEE Intelligent Vehicles Symposium (IV)*, pages 858–863, 2016.
- [2] Paul Verlaine Gakne and Kyle O’Keefe. Tightly-coupled gnss/vision using a sky-pointing camera for vehicle navigation in urban areas. *Sensors*, 18(4):1244, 2018.
- [3] Y. Yu, W. Gao, C. Liu, S. Shen, and M. Liu. A gps-aided omnidirectional visual-inertial state estimator in ubiquitous environments. In *2019 IEEE/RSJ International Conference on Intelligent Robots and Systems (IROS)*, pages 7750–7755, 2019.
- [4] W. Lee, K. Eickenhoff, P. Geneva, and G. Huang. Intermittent gps-aided vio: Online initialization and calibration. In *2020 IEEE International Conference on Robotics and Automation (ICRA)*, pages 5724–5731, 2020.
- [5] J. Rehder, K. Gupta, S. Nuske, and S. Singh. Global pose estimation with limited gps and long range visual odometry. In *2012 IEEE International Conference on Robotics and Automation*, pages 627–633, 2012.
- [6] R. Mascaro, L. Teixeira, T. Hinzmann, R. Siegwart, and M. Chli. Gomsf: Graph-optimization based multi-sensor fusion for robust uav pose estimation. In *2018 IEEE International Conference on Robotics and Automation (ICRA)*, pages 1421–1428, 2018.
- [7] Wenlin Yan, Luísa Bastos, José A Gonçalves, Américo Magalhães, and Tianhe Xu. Image-aided platform orientation determination with a gnss/low-cost imu system using robust-adaptive kalman filter. *GPS Solutions*, 22(1):12, 2018.
- [8] Tong Qin, Shaozu Cao, Jie Pan, and Shaojie Shen. A general optimization-based framework for global pose estimation with multiple sensors, 2019.
- [9] W. Wen, X. Bai, Y. C. Kan, and L. Hsu. Tightly coupled gnss/ins integration via factor graph and aided by fish-eye camera. *IEEE Transactions on Vehicular Technology*, 68(11):10651–10662, 2019.
- [10] Dae Hee Won, Eunsung Lee, Moonbeom Heo, Sangkyung Sung, Jiyun Lee, and Young Jae Lee. Gnss integration with vision-based navigation for low gnss visibility conditions. *GPS solutions*, 18(2):177–187, 2014.
- [11] Dae Hee Won, Eunsung Lee, Moonbeom Heo, Seung-Woo Lee, Jiyun Lee, Jeongrae Kim, Sangkyung Sung, and Young Jae Lee. Selective integration of gnss, vision sensor, and ins using weighted dop under gnss-challenged environments. *IEEE Transactions on Instrumentation and Measurement*, 63(9):2288–2298, 2014.
- [12] Tuan Li, Hongping Zhang, Zhouzheng Gao, Xiaoji Niu, and Naser El-Sheimy. Tight fusion of a monocular camera, mems-imu, and single-frequency multi-gnss rtk for precise navigation in gnss-challenged environments. *Remote Sensing*, 11(6):610, 2019.
- [13] G. Huang. Visual-inertial navigation: A concise review. In *2019 International Conference on Robotics and Automation (ICRA)*, pages 9572–9582, 2019.
- [14] Weisong Wen, Tim Pfeifer, Xiwei Bai, and Li-Ta Hsu. It is time for factor graph optimization for gnss/ins integration: Comparison between FGO and EKF. *CoRR*, 2020.
- [15] Zheng Gong, Rendong Ying, Fei Wen, Jiuchao Qian, and Peilin Liu. Tightly coupled integration of gnss and vision slam using 10-dof optimization on manifold. *IEEE Sensors Journal*, 19(24):12105–12117, 2019.
- [16] T. Qin, P. Li, and S. Shen. Vins-mono: A robust and versatile monocular visual-inertial state estimator. *IEEE Transactions on Robotics*, 34(4):1004–1020, 2018.
- [17] Gang Xie et al. Principles of gps and receiver design. *Publishing House of Electronics Industry, Beijing*, 7:61–63, 2009.
- [18] K. J. Wu, C. X. Guo, G. Georgiou, and S. I. Roumeliotis. Vins on wheels. In *2017 IEEE International Conference on Robotics and Automation (ICRA)*, pages 5155–5162, 2017.
- [19] S. Ch’ng, A. Khosravian, A. Doan, and T. Chin. Outlier-robust manifold pre-integration for ins/gps fusion. In *2019 IEEE/RSJ International Conference on Intelligent Robots and Systems (IROS)*, pages 7489–7496, 2019.
- [20] Sameer Agarwal, Keir Mierle, and Others. Ceres solver. <http://ceres-solver.org>.
- [21] Stefan Leutenegger, Simon Lynen, Michael Bosse, Roland Siegwart, and Paul Furgale. Keyframe-based visual-inertial odometry using non-linear optimization. *The International Journal of Robotics Research*, 34(3):314–334, 2015.
- [22] J. Liu, W. Gao, and Z. Hu. Visual-inertial odometry tightly coupled with wheel encoder adopting robust initialization and online extrinsic calibration. In *2019 IEEE/RSJ International Conference on Intelligent Robots and Systems (IROS)*, pages 5391–5397, 2019.
- [23] W. Wen, Y. Zhou, G. Zhang, S. Fahandezh-Saadi, X. Bai, W. Zhan, M. Tomizuka, and L. T. Hsu. Urbanloco: A full sensor suite dataset for mapping and localization in urban scenes. In *2020 IEEE International Conference on Robotics and Automation (ICRA)*, pages 2310–2316, 2020.
- [24] T Takasu. Rtklib: An open source program package for gnss positioning. *Tech. Rep.*, 2013. *Software and documentation*, 2011.
- [25] J. Sturm, N. Engelhard, F. Endres, W. Burgard, and D. Cremers. A benchmark for the evaluation of rgb-d slam systems. In *2012 IEEE/RSJ International Conference on Intelligent Robots and Systems*, pages 573–580, 2012.